Laser–Plasma Interactions in Direct-Drive–Ignition Plasmas

Introduction

Two approaches to inertial confinement fusion (ICF)[1] employ megajoule-class laser beams[2,3] to compress a fusion capsule to thermal nuclear burn. For the indirect-drive approach,[4] the laser beams are tightly focused through the laser entrance hole into a radiation cavity (hohlraum) resulting in relatively high single-beam laser intensities ($I_s \sim 10^{15}$ W/cm^2). The beams then propagate through a series of plasmas before converting their energy into soft x-ray radiation at the high-Z hohlraum wall.[5–8] The soft x-ray radiation emitted by the hohlraum illuminates a fusion capsule and the ablated material drives a spherical implosion.[4,9] As the high-intensity laser beams propagate to the hohlraum wall, they encounter millimeter-scale-length plasmas that make them particularly susceptible to laser–plasma instabilities[10] that reduce the x-ray drive. This is in contrast to the direct-drive approach,[11] where laser beams directly illuminate the fusion capsule and it is the overlapped laser beam intensity ($I_{ovr} \sim 10^{15}$ W/cm^2) that launches a series of shocks to compress the nuclear fuel to fusion conditions.[12] As laser beams propagate up the density gradient to the critical surface (Fig. 132.1), they are susceptible to several laser–plasma instabilities that can divert their energy, thereby reducing the hydrodynamic efficiency [$\epsilon = (1/2\, mv^2)/E_{laser}$, where m is the mass of the imploding shell, v is the implosion velocity, and E_{laser} is the total laser energy] or the symmetry of the drive. Direct drive is most susceptible to laser–plasma instabilities that depend on multiple laser beams, as the peak single-beam intensities are relatively low ($I_s \approx 8/NI_{ovr}$, where N is the total number of laser beams illuminating the capsule) and the coronal electron temperatures are high ($T_e \simeq 3.5$ keV). Cross-beam energy transfer (CBET)[13] and two-plasmon decay (TPD)[14] are two such instabilities that are driven by the intensities of multiple laser beams.

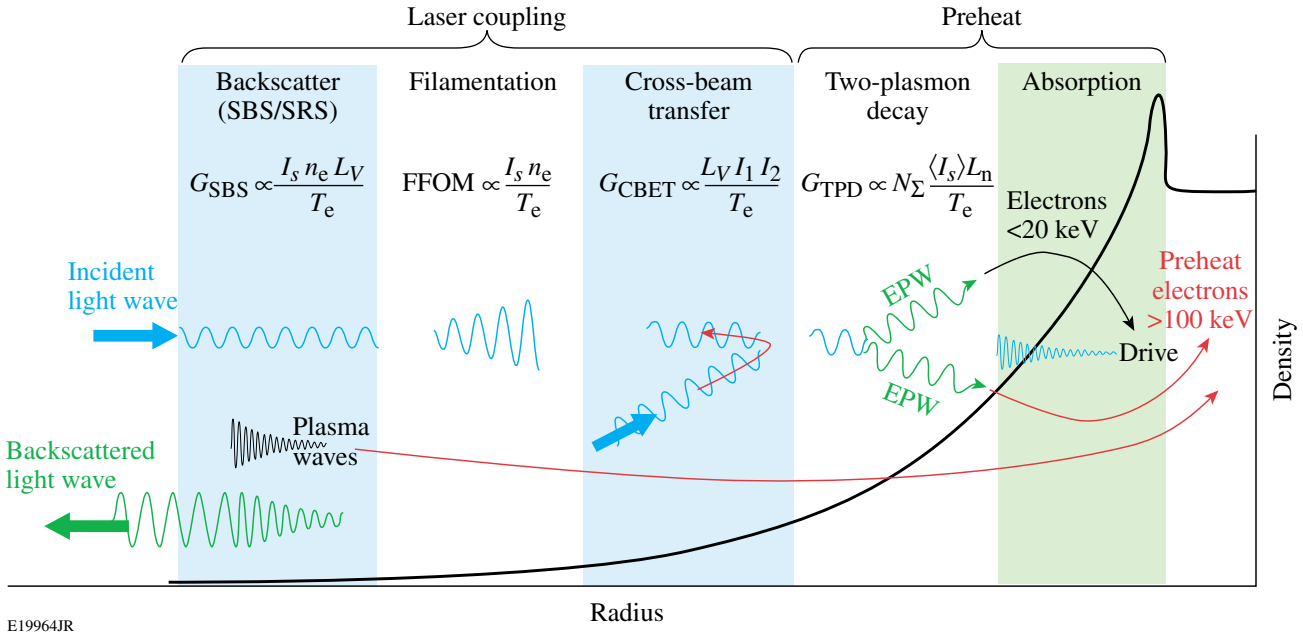

Figure 132.1
Schematic of the direct-drive density profile and potential laser–plasma interactions encountered by incident direct-drive beams. As a result of the relatively low single-beam intensities (I_s), direct-drive experiments are most susceptible to the laser-beam instabilities that are driven by multiple laser beams (e.g., CBET, TPD).

CBET is a mechanism that reduces the hydrodynamic efficiency in high-energy-density laser experiments.[15–19] For direct-drive fusion experiments [Fig. 132.2(a)], CBET was identified by linking discrepancies in the scattered-light spectrum to a lack of energy penetrating to the critical surface.[20] CBET results from large-amplitude ion-acoustic waves [Fig. 132.2(b)] driven by the laser light (k_2) that propagates past the target, seeding stimulated Brillouin scattering[21] along the light from the opposing laser beams (k_1). The enhanced ion-acoustic waves scatter light primarily from the central rays of the incident laser beams to the lower-energy outgoing rays. CBET is driven by the product of the intensity of the crossing beams near the Mach-1 surface.

Experiments focusing on TPD at direct-drive–ignition conditions[22] have shown that the efficiency of hot-electron generation scales with the overlapped laser-beam intensity, and experiments have demonstrated that multiple laser beams can share a common TPD electron plasmon wave.[23,24] The resonant common electron plasma waves are restricted to a region bisecting the laser beams [Fig. 132.2(c)], and the measured efficiency of the hot-electron generation scales rapidly with the maximum convective multibeam (intensity) gain[24,25]

$$G_{\mathrm{MB}} = 2.1\times 10^{-16} N_{\Sigma} f_g \frac{\langle I_{s,\mathrm{q}}\rangle [\mathrm{W/cm}^2] L_{\mathrm{n,q}}[\mu\mathrm{m}]}{T_{\mathrm{e,q}}[\mathrm{keV}]}, \qquad (1)$$

where N_{Σ} is the number of laser beams that share a common angle with the primary electron plasma wave, $\langle I_{s,\mathrm{q}}\rangle$ is the average single-beam intensity, $L_{\mathrm{n,q}}$ is the density scale length, $T_{\mathrm{e,q}}$ is the electron temperature, and q denotes the fact that these parameters are taken at the quarter-critical surface of the laser beams. The factor f_g is determined by the geometry and polarization of the laser beams.[24,25] The geometric factor and the number of symmetric beams are constant for a given configuration, resulting in a common-wave gain proportional to the overlapped laser-beam intensity.

The linear gain calculations provide general guidance for the TPD threshold but the instability is inherently nonlinear. To study the nonlinear behavior of TPD, simulations based on a nonlinear Zakharov model[26] were performed. *ZAK*[27] is a plasma-fluid model that incorporates saturation nonlinearities including density-profile modification,[28] Langmuir wave cavitation,[29] and the generation of ion-acoustic turbulence.[27,30] *ZAK* simulations can describe the growth and nonlinear saturation of the instability but do not include kinetic effects responsible for hot-electron generation. The generalization of the *ZAK* model, *QZAK*,[31–33] accounts for kinetic effects self-consistently in the quasi-linear approximation. The addition of kinetic effects reduces the amplitude of the electron plasma waves for a given $I_{\mathrm{q}} L_{\mathrm{n,q}} / T_{\mathrm{e,q}}$. These models provide a physics-based capability for calculating TPD at ignition conditions and a method for studying different mitigation techniques in this highly nonlinear process.

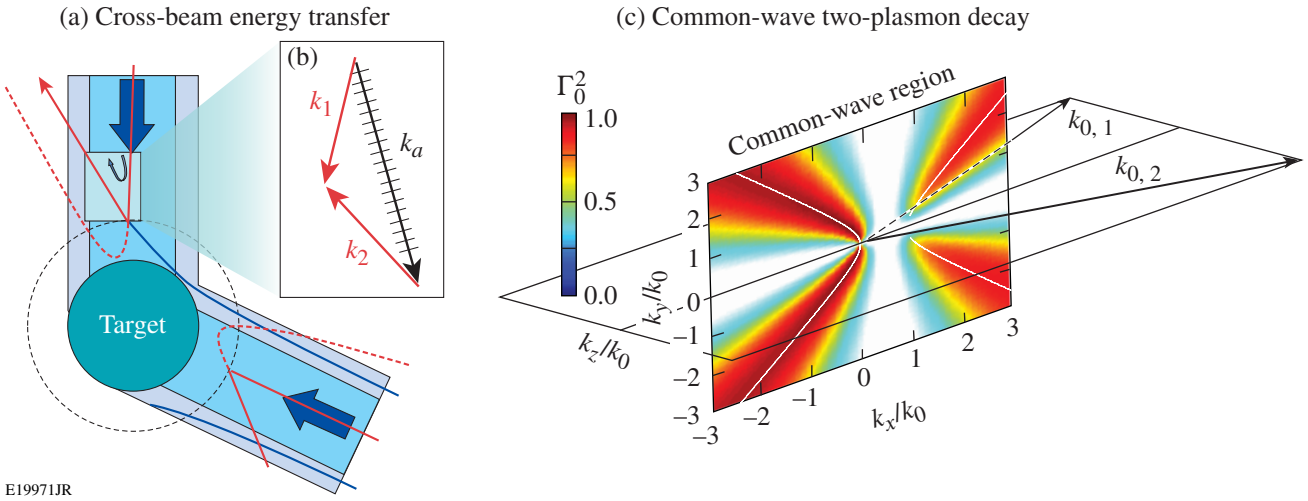

Figure 132.2
(a) Light rays propagating past the target (blue) interact with light rays in the central region of another beam (red). The interacting light rays seed an ion-acoustic wave near the Mach-1 surface (dashed circle). The ion-acoustic wave scatters light before it can penetrate deep into the target (dashed red curves). (b) A wave-vector diagram showing a typical matching condition for CBET. (c) The common-wave TPD growth rate $\left(\Gamma_0^2\right)$ for two OMEGA EP beams that are polarized in the vertical direction (k_y) is plotted in the resonant common-wave region; the common-wave region bisects the laser beams.

Underdense Hydrodynamics

To understand and mitigate the effect of laser–plasma instabilities, it is necessary to characterize the plasma conditions. The laser-intensity threshold for the onset of these instabilities must be taken into account in the design of fusion experiments; small variations in the plasma conditions can greatly impact target performance. Numerous laser–plasma instability studies over the past 20 years have emulated plasma conditions that will be achieved in fusion targets at the National Ignition Facility (NIF).[34–37] Generally, these studies have shown the strong sensitivity of laser–plasma interactions to the exact plasma conditions, highlighting the importance of correctly modeling the underdense plasma. Ultraviolet Thomson scattering provides access to the high densities prevalent in ICF coronal plasmas and is now routinely used as a diagnostic to characterize the electron and ion temperatures.[38–40]

The Thomson-scattering diagnostic on OMEGA employs a 20-J, $\lambda_{4\omega} = 0.26$-μm probe beam.[41] The Thomson-scattered light is collected from a $60 \times 75 \times 75$-mm volume defined by the 60-μm best-focus diameter of the probe beam, the 150-μm-wide spectrometer slit, and the 150-μm-wide streak camera slit.[40,42] The Thomson-scattering diagnostic probes ion-acoustic waves with a wave number $k_a = 2k_{4\omega} \sin(\theta/2)$, where $k_{4\omega} = 2\pi/\lambda_{4\omega}$ and $\theta = 63°$ is the scattering angle.

1. Hydrodynamic Modeling

The direct-drive–implosion experiments are designed using the 1-D hydrodynamics code *LILAC*,[43] which implements a nonlocal heat transport model[44] and a CBET model.[18,19] The CBET model is incorporated into the laser-absorption package, allowing for a self-consistent calculation of laser deposition with CBET. The model considers pairwise interactions of pump light rays with probe light rays and all possible crossings of these rays within the corona plasma. A spatial gain is estimated in the strong damping limit to calculate the energy transfer.

To reproduce the measured laser coupling and the measured hydrodynamic efficiency, both the nonlocal transport and CBET models must be used. The laser coupling is characterized by time-dependent absorption fraction, inferred from scattered-light measurements and the scattered-frequency spectrum.[20] When a flux-limited transport model is used, critical features in the scattering spectrum are not reproduced indicating that the time-dependent coronal conditions have not been simulated correctly. Simulations performed using the nonlocal transport model, but without CBET, drove the implosion too efficiently; the simulated bang time was ~200 ps earlier than measured, which is consistent with the lower shell-trajectory measurements inferred from x-ray self-emission images of the imploding targets.[45]

2. Spherical Geometry

Figure 132.3(a) shows the Thomson-scattering spectra obtained from two shots where 860-μm-diam capsules with 27-μm-thick carbon–hydrogen (CH) walls filled with 10 atm of D_2 gas were driven by a laser pulse consisting of three picket pulses followed by a main drive pulse at $I_{ovr} = 3 \times 10^{14}$ W/cm^2 (Ref. 12). Nearly 0.7 ns after the initial picket illuminated the target, the plasma has expanded to the Thomson-scattering volume located 400 μm from the initial target surface. Two characteristic ion-acoustic features were observed and, to obtain the plasma conditions, the spectra were fit [Fig. 132.3(b)] every 50 ps using a standard theoretical form factor.[46] The light scattered from the ion-acoustic waves was further blue shifted as a result of the outward plasma-flow velocity [Fig. 132.3(d)]; the ion-acoustic wave vectors (k_a) are aligned in the radial direction. The relative amplitude of the ion-acoustic features provides a measure of the drift between the ions and electrons near the phase velocity of the ion-acoustic waves [Fig. 132.3(d)].[46] This drift velocity was caused by the plasma maintaining quasi-neutrality as "fast" heat carrying electrons move outward.

The spectral feature nearest the wavelength of the probe [top feature in Fig. 132.3(a) and expanded in Fig. 132.4(a)] results from light in the wings of the probe beam that is reflected from the plasma; this turning point, located near the 3ω critical surface (the turning point has moved below the 4ω critical density as a result of the glancing incidence of the probe beam), is a result of the 60° angle between the probe beam and the target normal. Figure 132.4(b) shows the calculated spectrum obtained by propagating 4ω light through the simulated plasma conditions. The wavelength shift provides a measure of the changing path length along the probe beam caused by the rapidly changing density[47] and the Doppler shift induced by the moving turning point. The intensity modulation is a result of absorption; between the pickets, the plasma rapidly cools and the probe light is absorbed. These measurements provide a powerful set of criteria to assess the hydrodynamic models used to design direct-drive–fusion experiments and to study laser–plasma instabilities.

3. Planar Geometry

To validate the plasma conditions calculated in planar geometry and used to interpret the two-plasmon–decay results, Thomson-scattering measurements were obtained on OMEGA[48] using the same target platform, pulse shape, and

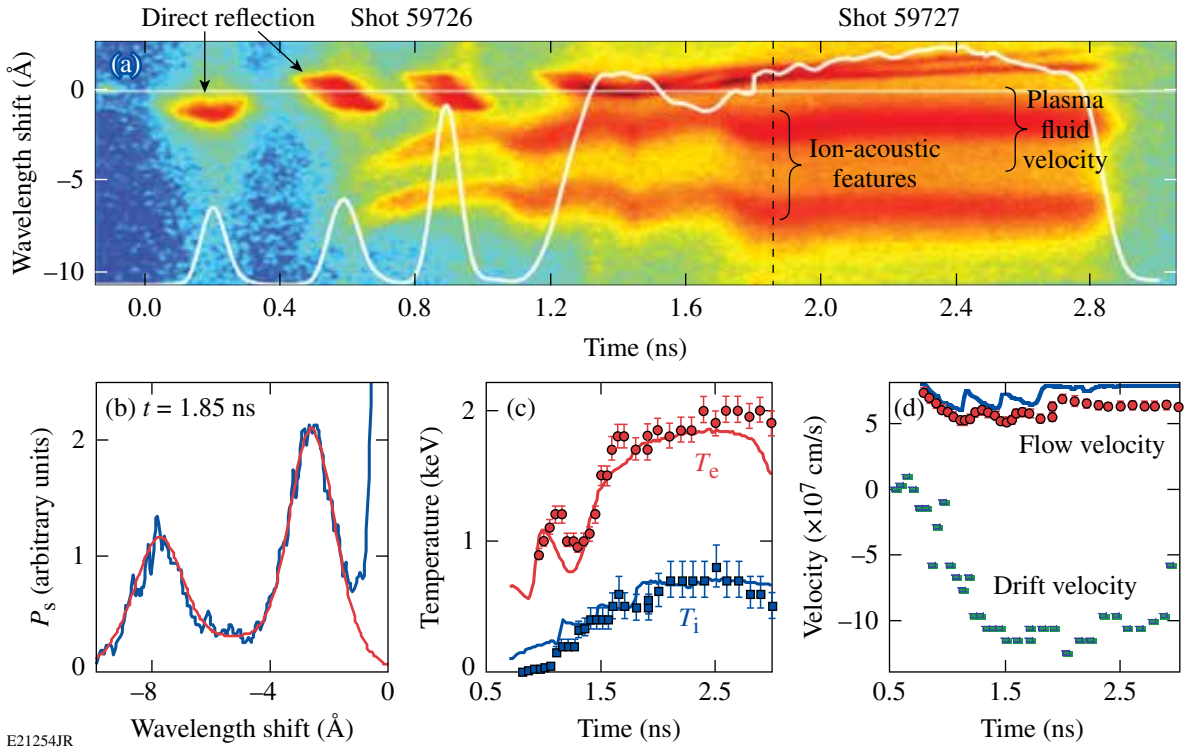

Figure 132.3
(a) The time-resolved Thomson-scattering spectrum obtained from the direct-drive coronal plasma. The pulse shape of the 3ω drive beams is shown (white curve). The Thomson-scattering probe beam was on over nearly the entire record (–0.1 ns to 2.8 ns). (b) The spectrum at 1.85 ns was fit to obtain the electron temperature, flow velocity, and drift velocity. The measured (c) electron temperature and (d) flow and drift velocities are plotted as a function of time. The solid curves are from 1-D hydrodynamic simulations that included nonlocal heat transfer and CBET models.

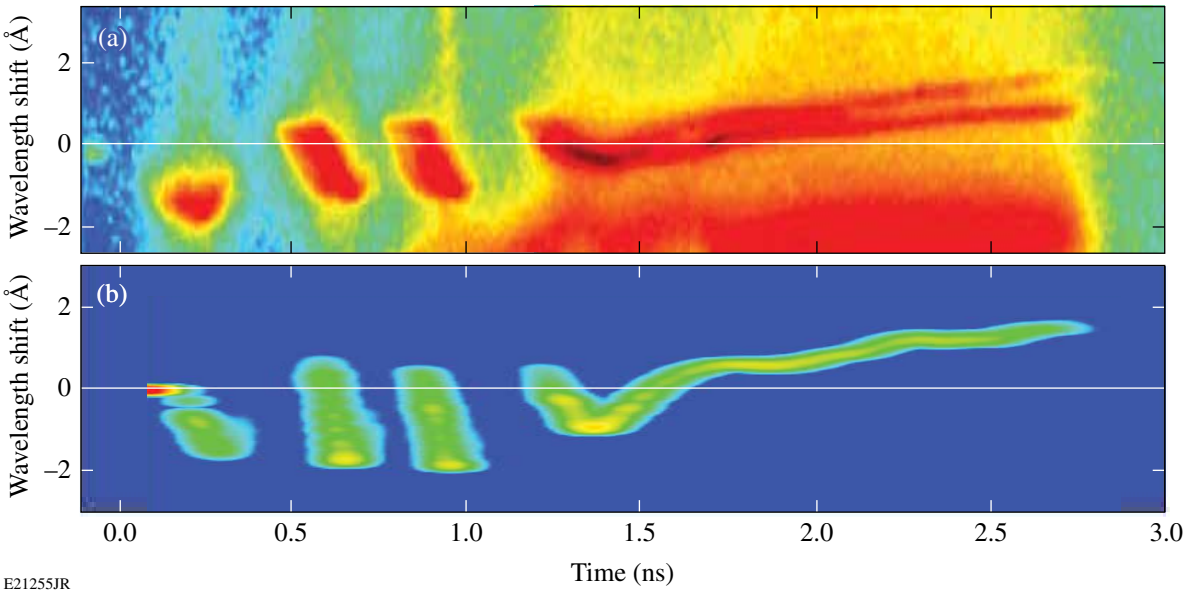

Figure 132.4
(a) The scale from Fig. 132.3(a) was expanded to highlight the spectrum obtained from light reflecting from the target surface. (b) The reflected light was modeled using the simulated plasma conditions.

similar laser beam diameters (490-μm FWHM) as used on the OMEGA EP[49] planar experiments discussed in **Two-Plasmon Decay** (p. 186). The planar targets consist of a 30-μm-thick CH layer deposited on 30-μm-thick molybdenum (Mo). Figure 132.5 shows the electron and ion temperatures as functions of time at the 3ω quarter-critical surface. The wavelength separation is a function of the ion-acoustic sound speed that leads to the direct measure of the electron temperature shown in Fig. 132.3(c). The multiple ion-acoustic modes present in the CH plasma provide an accurate measure of the ion temperature.[50] There is excellent agreement with the 2-D hydrodynamic simulations using the code *DRACO*.[51] Furthermore, the rarefaction wave launched from the CH–Mo interface is observed in the Thomson-scattering spectrum 1.11 ns after the laser beams turn on, which is in agreement with the hydrodynamic simulations. This agreement demonstrates the accuracy of the thermal-conduction model and is a strong indication that the calculated density and temperature profiles are accurate.

Cross-Beam Energy Transfer

1. CBET Experiments

To reduce CBET and increase the implosion velocity in direct-drive experiments, the energy in the rays that bypass the target was reduced by decreasing the radii of the laser beams (R_b) relative to the target radius ($R_t = 430$ μm). Figure 132.6(a) shows that, when the radii of the laser beams are reduced from $R_b/R_t = 1.1$ to 0.75, the measured absorption is increased from 68% to 87% (Ref. 52). This results in an increase in the implosion velocity from 160 to 195 km/s [Fig. 132.6(b)]. Simulations that include both nonlocal heat transport[44] and CBET models[19] developed in the 1-D hydrodynamic code *LILAC* (see **Hydrodynamic Modeling**, p. 183) are in excellent agreement with the measurements shown in Fig. 132.6.

When the CBET model is not included in the simulations, both the absorption and hydrodynamic efficiency increase by ~15% as the tighter focused laser spots direct more energy on target [Fig. 132.6(b)]. This is in contrast to the measured ~35% increase in the hydrodynamic efficiency; a factor of 2 larger than the measured 15% increase in absorption. This enhanced hydrodynamic efficiency is a direct result of reducing CBET, which increases the energy in the central portion of the laser beams, leading to more energy deposited near the critical surface.

Although the hydrodynamic efficiency is significantly increased, reducing the radii of the laser beams with respect to the target radius introduces a nonuniform illumination on the initial target surface [Fig. 132.6(c)], which can lead to low-mode nonuniformities and reduced implosion performance. Figure 132.6(c) shows that the root-mean-square (rms) deviation from the average shell radius (nonuniformities), measured near the ablation front [Fig. 132.6(d)],[45] increased from less than 5 μm to greater than 25 μm as the laser radii were reduced from $R_b/R_t = 1.1$ to 0.5 (Ref. 52).

2. Mitigation of Cross-Beam Energy Transfer

To mitigate CBET and maintain sufficient illumination uniformity in direct-drive implosions, a two-state zooming has been proposed.[53] During the critical time for seeding nonuniformities (laser imprint), before a significant conduction zone is produced, the radii of the laser beams are equal to the target

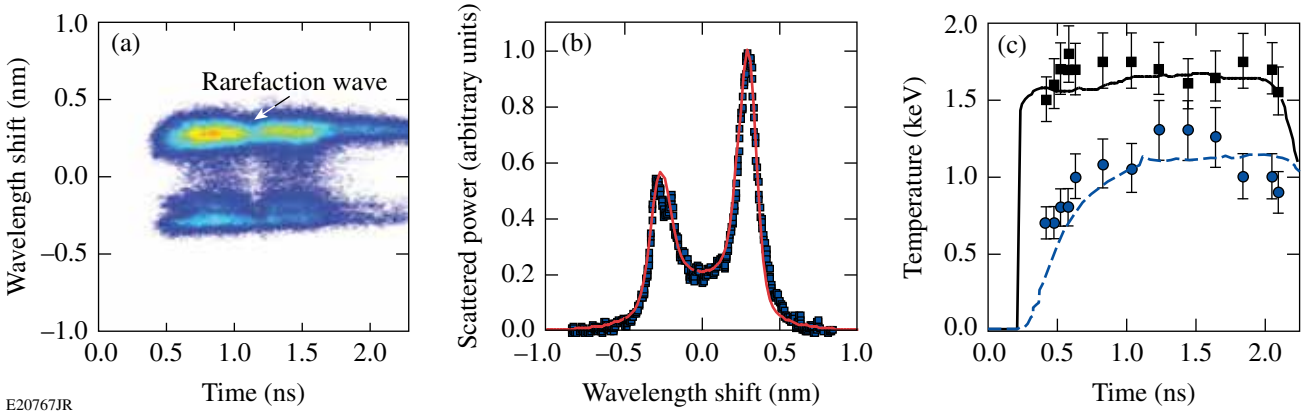

Figure 132.5
(a) The Thomson-scattering spectrum obtained from scattering at the 3ω quarter-critical surface in planar geometry for a drive intensity of $I_{ovr} = 3 \times 10^{14}$ W/cm^2. (b) The spectrum at 0.8 ns is fit to obtain a $T_e = 1.6$ keV and $T_i = 1.0$ keV. (c) The electron (squares) and ion (circles) temperatures are plotted as a function of time and compared with 2-D hydrodynamic modeling.

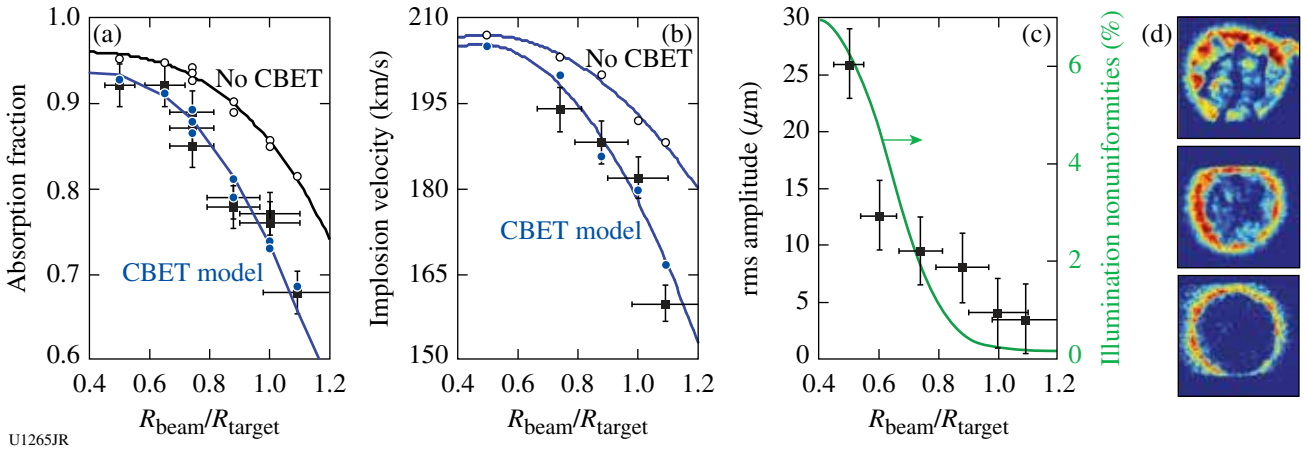

Figure 132.6

(a) The absorbed light, (b) implosion velocity, and (c) rms deviation from the average shell radius (left axis), along with the calculated illumination nonuniformities (right axis) are plotted as functions of the ratio between the laser-beam and target radius. The simulation results that include the CBET model (solid circles) are in excellent agreement with the measurements. Simulations performed without the CBET model (open circles) significantly overestimate the absorbed light and the implosion velocity. (d) X-ray self-emission images are used to determine the nonuniformities at a constant capsule radius of 175 μm; the soft x rays emitted from the ablation surface (outer edge of the imploding shell) were measured for three focus conditions: R_b/R_t = 0.5, 0.75, and 1.0 (from top to bottom).

radius $\left(R_b/R_t = 1.0\right)$, minimizing the laser imprint. Once the plasma has sufficiently expanded, the radii of the laser beams are reduced $\left(R_b/R_t = 0.7\right)$, minimizing CBET. The increase in transverse thermal conduction smooths the low-mode intensity nonuniformities, producing a uniform drive. Initial 2-D hydrodynamic simulations of OMEGA direct-drive experimental conditions indicate that transitioning to smaller laser spots after the picket pulses does not increase the low-mode nonuniformities.[54] The combination of zooming and dynamic bandwidth reduction (removing smoothing by spectral dispersion during the drive[55]) could provide a 30% effective increase in the drive energy for OMEGA direct-drive implosions.

Potential schemes to achieve zooming of the focal spot on target involve modifications to the spatial coherence of the laser that causes broadening in the far field of the laser beams. One method suitable for most high-power laser systems employs a radially varying zoom phase plate (ZPP) and a two-state dynamic near-field profile. The ZPP's central area would produce a large focal spot, while the outer area would produce a smaller focal spot. During the picket pulses, a small-diameter near-field beam propagates through the center region of the ZPP forming a large diameter on-target spot. During the drive pulse, an annulus-shaped near-field profile propagates through the outer region of the ZPP producing a smaller-diameter on-target spot.[56,57]

Two-Plasmon Decay

The large-diameter targets (~3 mm) and moderate overlapped laser intensities ($I_{ovr} \sim 7 \times 10^{14}$ W/cm^2, $I_{s,q} \lesssim 10^{14}$ W/cm^2) proposed for direct-drive–ignition experiments will produce high-temperature ($T_{e,q} \sim 3.5$ keV), long-scale-length ($L_{n,q} \sim 500\ \mu$m) underdense plasmas.[58] Multibeam linear gain calculations [Eq. (1)] and recent results[25] from OMEGA suggest that TPD will be near threshold where details in the exact hydrodynamic conditions and beam pointings may play a significant role in the number of hot electrons produced by TPD. A fraction of the hot electrons produced by two-plasmon decay will be absorbed into the unablated fuel ("preheat"), and may increase the implosion adiabat and reduce the compression efficiency. Typical direct-drive–ignition designs can withstand of the order of 0.1% of the laser energy converted to preheat.[59]

Figure 132.7 shows the results from a series of experiments in planar and spherical geometries that were designed to account for all of the hot electrons generated by TPD.[60] The coupling of these hot electrons to a fusion target (preheat) will be reduced by the electron divergence, the distance between where the electrons are created and where they are absorbed, the energy distribution of the electrons (T_{hot}), and other loss mechanisms. The experiments on OMEGA EP employed a single cone of four beams (23° from the target normal) with ~860-μm FWHM laser spots; the planar experiments on

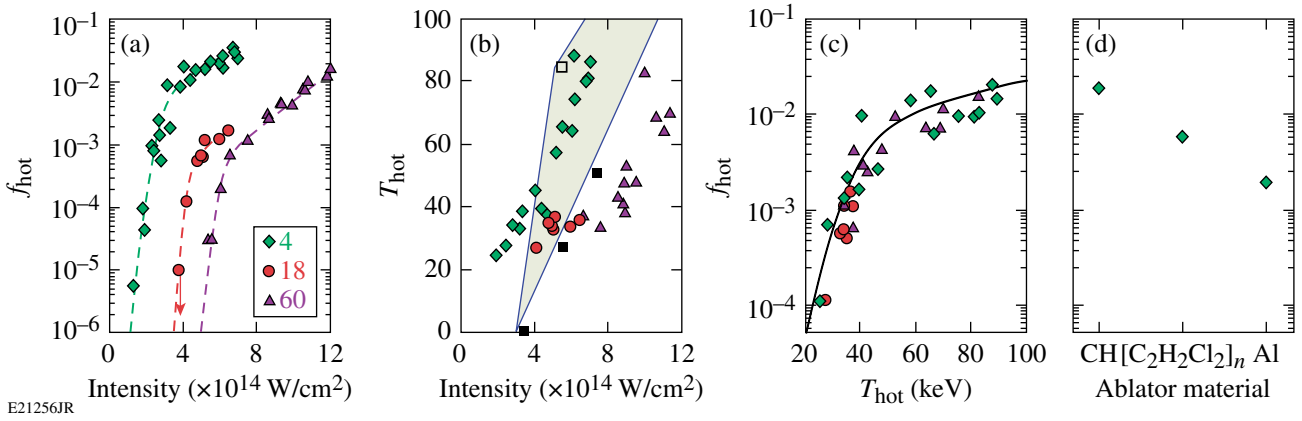

Figure 132.7
(a) The fraction of laser energy converted to hot electrons (f_{hot}) and (b) the hot-electron temperature (T_{hot}) are shown for three beam geometries: four-beam planar (diamonds), 18-beam planar (circles), and 60-beam spherical (triangles) as a function of the vacuum overlapped intensities (I_{ovr}). The hot-electron temperatures calculated by *ZAK* (open squares) and *QZAK* (solid squares) are included for reference. (c) The hot-electron fraction is plotted as a function of the hot-electron temperature for the three target geometries. (d) The f_{hot} measured on the four-beam planar configuration is plotted for a series of ablator materials for a vacuum overlapped intensity of 7×10^{14} W/cm^2.

OMEGA consisted of 18 beams with 710-μm FWHM laser spots in three cones (six at 23°, six at 48°, and six at 60° from the target normal); the spherical experiments used 60 beams and the target diameter was matched to the diameter of the laser spots, where 95% of the laser power illuminates the initial target surface ($R_t = 865$ μm). Each target geometry has its own intensity threshold as a result of the differences in the number of beams that contribute to the common electron plasma wave, scale lengths, electron temperatures, and the geometric factor as indicated in Eq. (1) (see Table 132.I). The hot-electron intensity thresholds shown in Fig. 132.7(a) suggest that the multibeam TPD gain [Eq. (1)] must be greater than $G_{MB} \approx 2$ for a measurable fraction of hot electrons ($f_{hot} \approx 10^{-5}$ is near the detection threshold).

1. Total Hot-Electron Fraction

To study TPD at ignition-relevant plasma conditions, the four ultraviolet (3ω, $\lambda = 0.35$ μm) beams available from OMEGA EP produced the required intensities ($I_{ovr} = 7 \times 10^{14}$ W/cm^2) over a large-diameter laser spot to create 400-μm plasma density scale lengths and $T_e = 2.5$-keV electron temperatures at $n_{cr}/4$. The long-scale-length CH plasma was produced by illuminating a 30-μm-thick CH layer deposited on 30 μm of Mo. The total energy in hot electrons was determined by measuring the K_α yield and the hot-electron temperature.[60]

Figure 132.7(a) shows that the fraction of laser energy converted into hot electrons scales exponentially over nearly three orders of magnitude when the vacuum overlapped intensity is increased from 1.3 to 3×10^{14} W/cm^2 and continues to grow at a slower rate as the intensity is extended to 7×10^{14} W/cm^2 (Ref. 61). The large fraction of laser energy converted into hot electrons along with its observed saturation is a direct consequence of the simultaneous high intensities and long-scale lengths ($L_{n,q} = 400$ μm) in these experiments. Previous TPD studies have shown saturation of the hot-electron generation at 0.1% of the incident laser energy when plotted against the vacuum laser intensity. This apparent saturation and low level of electron generation results from the hydrodynamics; the small laser spots used to produce the highest intensities limited the

Table 132.I: Estimates of the factors used to calculate the common-wave gain at the threshold intensity for each configuration shown.

Configuration	f_g	$N_\Sigma \langle I_{s,q} \rangle$	$L_{n,q}/T_{e,q}$	I_{ovr}^{th}	G_{MB}^{th}
4 beam	0.5	~1/2 I_{ovr}	~170 μm/keV	~2	1.7
18 beam	0.5	~1/4 I_{ovr}	~135 μm/keV	~4	1.4
60 beam	0.5	~1/2 I_{ovr}	~60 μm/keV	~5	1.5

scale length to $L_{n,q} < 200\ \mu$m (Ref. 23). The highest intensity corresponds to a TPD gain larger than those estimated for direct-drive–ignition experiments and the fraction of these electrons that are deposited as preheat in the fuel will be significantly reduced as a result of their divergence and energies.

2. Hot-Electron Temperature (T_{hot})

Figure 132.7(b) shows that, for a given target geometry, the hot-electron temperature scales with the vacuum intensity. The four-beam planar experimental results are compared with the code *ZAK*.[27] While this plasma-fluid model describes the growth and nonlinear saturation of the instability, it does not include kinetic effects responsible for hot-electron generation. An estimate for the hot-electron temperature was instead obtained from the nonlinearly saturated state via the integration of test-electron trajectories in the electrostatic fields associated with the Langmuir turbulence (see Ref. 27 for more details). The solid triangles in Fig. 132.7 show the results of the *QZAK* model where kinetic effects are taken into account self-consistently in the quasi-linear approximation.[62] The addition of kinetic effects lowers the amplitude of the electron plasma waves, reducing the hot-electron temperature for a given $I_q L_{n,q}/T_{e,q}$. The difference between the two model predictions highlights the difficulty in making predictive calculations of a highly turbulent and complex physical system.

Figure 132.7(c) shows the measured correlation, for all three target geometries, between the hot-electron temperature and the fraction of laser energy converted to hot electrons. The fact that each target geometry has its own intensity threshold, even though the hot-electron generation plotted as a function of hot-electron temperature shares a common curve, suggests that the differences in thresholds [Fig. 132.7(b)] result from the laser beam coupling to the TPD instability.[25]

Mitigation of Two-Plasmon Decay

Figure 132.7(d) shows the fraction of hot electrons generated by TPD for various ablator materials measured on OMEGA EP at a vacuum overlapped intensity of 7×10^{14} W/cm^2. Although some of the reduction in the fraction of hot electrons is a result of the changing hydrodynamics (i.e., increased T_e, reduced L_n), recent particle-in-cell simulations indicate a sensitivity of TPD to the electron–ion collisions,[63] and it is plausible that reducing the ion-acoustic wave damping will lead to a reduced TPD saturation level. Previous implosion experiments using silicon dioxide (SiO_2) ablators have observed a significant reduction in the fraction of laser energy converted to hot electrons,[64] and more-recent hydrodynamic studies of direct-drive–implosion designs add Si/Ge doping to the CH ablator to reduce the Rayleigh–Taylor growth.[65,66]

Summary

A series of laser–plasma interaction experiments performed at the Omega Laser Facility have investigated CBET and TPD at direct-drive–ignition conditions. Direct-drive ignition is most susceptible to these multibeam instabilities because the single-beam intensities are low and the electron temperatures in the underdense plasma are high. These studies have led to mitigation strategies for both CBET and TPD; reducing the radii of the laser beams with respect to the target during the main drive minimizes CBET, and varying the ablator material suggests that the hot electrons produced by TPD can be significantly reduced.

ACKNOWLEDGMENT

We acknowledge the OMEGA EP and OMEGA operations teams whose efforts made these results possible. This work was supported by the U.S. Department of Energy Office of Inertial Confinement Fusion under Cooperative Agreement No. DE-FC52-08NA28302, the University of Rochester, and the New York State Energy Research and Development Authority. The support of DOE does not constitute an endorsement by DOE of the views expressed in this article.

REFERENCES

1. J. Nuckolls *et al.*, Nature **239**, 139 (1972).
2. E. I. Moses and C. R. Wuest, Fusion Sci. Technol. **47**, 314 (2005).
3. C. Cavailler, Plasma Phys. Control. Fusion **47**, B389 (2005).
4. J. D. Lindl *et al.*, Phys. Plasmas **11**, 339 (2004).
5. D. H. Froula, L. Divol, R. A. London, R. L. Berger, T. Döppner, N. B. Meezan, J. Ralph, J. S. Ross, L. J. Suter, and S. H. Glenzer, Phys. Plasmas **17**, 056302 (2010).
6. S. H. Glenzer *et al.*, Science **327**, 1228 (2010).
7. W. L. Kruer, *The Physics of Laser–Plasma Interactions*, Frontiers in Physics, Vol. 73, edited by D. Pines (Addison-Wesley, Redwood City, CA, 1988).
8. C. Labaune *et al.*, Plasma Phys. Control. Fusion **46**, B301 (2004).
9. S. H. Glenzer *et al.*, Plasma Phys. Control. Fusion **54**, 045013 (2012).
10. D. H. Froula, L. Divol, N. B. Meezan, S. Dixit, J. D. Moody, P. Neumayer, B. B. Pollock, J. S. Ross, and S. H. Glenzer, Phys. Rev. Lett. **98**, 085001 (2007); D. H. Froula, L. Divol, R. A. London, P. Michel, R. L. Berger, N. B. Meezan, P. Neumayer, J. S. Ross, R. Wallace, and S. H. Glenzer, Phys. Rev. Lett. **100**, 015002 (2008); D. H. Froula, Phys. Rev. Lett. **103**, 045006 (2009).

11. R. L. McCrory, D. D. Meyerhofer, R. Betti, R. S. Craxton, J. A. Delettrez, D. H. Edgell, V. Yu Glebov, V. N. Goncharov, D. R. Harding, D. W. Jacobs-Perkins, J. P. Knauer, F. J. Marshall, P. W. McKenty, P. B. Radha, S. P. Regan, T. C. Sangster, W. Seka, R. W. Short, S. Skupsky, V. A. Smalyuk, J. M. Soures, C. Stoeckl, B. Yaakobi, D. Shvarts, J. A. Frenje, C. K. Li, R. D. Petrasso, and F. H. Séguin, Phys. Plasmas **15**, 055503 (2008).

12. V. N. Goncharov, T. C. Sangster, T. R. Boehly, S. X. Hu, I. V. Igumenshchev, F. J. Marshall, R. L. McCrory, D. D. Meyerhofer, P. B. Radha, W. Seka, S. Skupsky, C. Stoeckl, D. T. Casey, J. A. Frenje, and R. D. Petrasso, Phys. Rev. Lett. **104**, 165001 (2010).

13. C. J. Randall, J. R. Albritton, and J. J. Thomson, Phys. Fluids **24**, 1474 (1981).

14. A. Simon, R. W. Short, E. A. Williams, and T. Dewandre, Phys. Fluids **26**, 3107 (1983).

15. R. K. Kirkwood *et al.*, Phys. Rev. Lett. **76**, 2065 (1996).

16. J. Myatt, A. V. Maximov, W. Seka, R. S. Craxton, and R. W. Short, Phys. Plasmas **11**, 3394 (2004).

17. P. Michel *et al.*, Phys. Rev. Lett. **102**, 025004 (2009).

18. I. V. Igumenshchev, D. H. Edgell, V. N. Goncharov, J. A. Delettrez, A. V. Maximov, J. F. Myatt, W. Seka, A. Shvydky, S. Skupsky, and C. Stoeckl, Phys. Plasmas **17**, 122708 (2010).

19. I. V. Igumenshchev, W. Seka, D. H. Edgell, D. T. Michel, D. H. Froula, V. N. Goncharov, R. S. Craxton, L. Divol, R. Epstein, R. Follett, J. H. Kelly, T. Z. Kosc, A. V. Maximov, R. L. McCrory, D. D. Meyerhofer, P. Michel, J. F. Myatt, T. C. Sangster, A. Shvydky, S. Skupsky, and C. Stoeckl, Phys. Plasmas **19**, 056314 (2012).

20. W. Seka, D. H. Edgell, J. P. Knauer, J. F. Myatt, A. V. Maximov, R. W. Short, T. C. Sangster, C. Stoeckl, R. E. Bahr, R. S. Craxton, J. A. Delettrez, V. N. Goncharov, I. V. Igumenshchev, and D. Shvarts, Phys. Plasmas **15**, 056312 (2008).

21. W. Seka, H. A. Baldis, J. Fuchs, S. P. Regan, D. D. Meyerhofer, C. Stoeckl, B. Yaakobi, R. S. Craxton, and R. W. Short, Phys. Rev. Lett. **89**, 175002 (2002).

22. W. Seka, D. H. Edgell, J. F. Myatt, A. V. Maximov, R. W. Short, V. N. Goncharov, and H. A. Baldis, Phys. Plasmas **16**, 052701 (2009).

23. C. Stoeckl, R. E. Bahr, B. Yaakobi, W. Seka, S. P. Regan, R. S. Craxton, J. A. Delettrez, R. W. Short, J. Myatt, A. V. Maximov, and H. Baldis, Phys. Rev. Lett. **90**, 235002 (2003).

24. D. T. Michel, A. V. Maximov, B. Yaakobi, S. X. Hu, J. F. Myatt, A. A. Solodov, R. W. Short, and D. H. Froula, "Experimental Demonstration of the Two-Plasmon-Decay Common-Wave Process," to be published in Physical Review Letters.

25. D. T. Michel, J. F. Myatt, A. V. Maximov, R. W. Short, J. A. Delettrez, S. X. Hu, I. V. Igumenshchev, W. Seka, A. A. Solodov, C. Stoeckl, B. Yaakobi, J. Zhang, and D. H. Froula, "Measured Multibeam Hot-Electron Intensity Threshold Quantified by a Two-Plasmon–Decay Resonant Common-Wave Gain in Various Experimental Configurations," submitted to Physics of Plasmas.

26. D. F. DuBois, D. A. Russell, and H. A. Rose, Phys. Rev. Lett. **74**, 3983 (1995).

27. J. F. Myatt, J. Zhang, J. A. Delettrez, A. V. Maximov, R. W. Short, W. Seka, D. H. Edgell, D. F. DuBois, D. A. Russell, and H. X. Vu, Phys. Plasmas **19**, 022707 (2012).

28. A. B. Langdon, B. F. Lasinski, and W. L. Kruer, Phys. Rev. Lett. **43**, 133 (1979).

29. G. D. Doolen, D. F. DuBois, and H. A. Rose, Phys. Rev. Lett. **54**, 804 (1985).

30. R. Yan, A. V. Maximov, C. Ren, and F. S. Tsung, Phys. Rev. Lett. **103**, 175002 (2009).

31. H. X. Vu, D. F. Dubois, D. A. Russell, and J. F. Myatt, "Hot-Electron Generation by Cavitating Langmuir Turbulence in the Nonlinear Stage of the Two-Plasmon–Decay Instability," submitted to Physics of Plasmas.

32. H. X. Vu, D. F. Dubois, D. A. Russell, and J. F. Myatt, "Hot-Electron Production and Suprathermal Heat Flux Scaling with Laser Intensity from the Two-Plasmon–Decay Instability," submitted to Physics of Plasmas.

33. J. F. Myatt, H. X. Vu, D. F. DuBois, D. A. Russell, J. Zhang, R. W. Short, A. V. Maximov, W. Seka, and D. H. Edgell, "Mitigation of Two-Plasmon Decay in Direct-Drive Inertial Confinement Fusion Through the Manipulation of Ion-Acoustic and Langmuir Wave Damping," to be submitted to Physics of Plasmas.

34. B. J. MacGowan *et al.*, Phys. Plasmas **3**, 2029 (1996).

35. J. C. Fernández *et al.*, Phys. Plasmas **7**, 3743 (2000).

36. E. Lefebvre *et al.*, Phys. Plasmas **5**, 2701 (1998).

37. D. H. Froula, L. Divol, N. B. Meezan, S. Dixit, P. Neumayer, J. D. Moody, B. B. Pollock, J. S. Ross, L. Suter, and S. H. Glenzer, Phys. Plasmas **14**, 055705 (2007).

38. S. H. Glenzer *et al.*, Rev. Sci. Instrum. **70**, 1089 (1999).

39. J. S. Ross, D. H. Froula, A. J. Mackinnon, C. Sorce, N. Meezan, S. H. Glenzer, W. Armstrong, R. Bahr, R. Huff, and K. Thorp, Rev. Sci. Instrum. **77**, 10E520 (2006).

40. D. H. Froula, J. S. Ross, L. Divol, and S. H. Glenzer, Rev. Sci. Instrum. **77**, 10E522 (2006).

41. A. J. Mackinnon, S. Shiromizu, G. Antonini, J. Auerbach, K. Haney, D. H. Froula, J. Moody, G. Gregori, C. Constantin, C. Sorce, L. Divol, R. L. Griffith, S. Glenzer, J. Satariano, P. K. Whitman, S. N. Locke, E. L. Miller, R. Huff, K. Thorp, W. Armstrong, W. Bahr, W. Seka, G. Pien, J. Mathers, S. Morse, S. Loucks, and S. Stagnitto, Rev. Sci. Instrum. **75**, 3906 (2004).

42. J. Katz, R. Boni, C. Sorce, R. Follett, M. J. Shoup III, and D. H. Froula, Rev. Sci. Instrum. **83**, 10E349 (2012).

43. J. Delettrez, Can. J. Phys. **64**, 932 (1986).

44. V. N. Goncharov, T. C. Sangster, P. B. Radha, R. Betti, T. R. Boehly, T. J. B. Collins, R. S. Craxton, J. A. Delettrez, R. Epstein, V. Yu. Glebov, S. X. Hu, I. V. Igumenshchev, J. P. Knauer, S. J. Loucks, J. A. Marozas, F. J. Marshall, R. L. McCrory, P. W. McKenty, D. D. Meyerhofer, S. P. Regan, W. Seka, S. Skupsky, V. A. Smalyuk, J. M. Soures, C. Stoeckl, D. Shvarts, J. A. Frenje, R. D. Petrasso, C. K. Li, F. Séguin, W. Manheimer, and D. G. Colombant, Phys. Plasmas **15**, 056310 (2008).

45. D. T. Michel, C. Sorce, R. Epstein, N. Whiting, I. V. Igumenshchev, R. Jungquist, and D. H. Froula, Rev. Sci. Instrum. **83**, 10E530 (2012).

46. D. H. Froula, S. H. Glenzer, N. C. Luhmann, and J. Sheffield, *Plasma Scattering of Electromagnetic Radiation: Theory and Measurement Techniques*, 2nd ed. (Academic Press, Burlington, MA, 2011).

47. T. Dewandre, J. R. Albritton, and E. A. Williams, Phys. Fluids **24**, 528 (1981).

48. T. R. Boehly, D. L. Brown, R. S. Craxton, R. L. Keck, J. P. Knauer, J. H. Kelly, T. J. Kessler, S. A. Kumpan, S. J. Loucks, S. A. Letzring, F. J. Marshall, R. L. McCrory, S. F. B. Morse, W. Seka, J. M. Soures, and C. P. Verdon, Opt. Commun. **133**, 495 (1997).

49. J. H. Kelly, L. J. Waxer, V. Bagnoud, I. A. Begishev, J. Bromage, B. E. Kruschwitz, T. J. Kessler, S. J. Loucks, D. N. Maywar, R. L. McCrory, D. D. Meyerhofer, S. F. B. Morse, J. B. Oliver, A. L. Rigatti, A. W. Schmid, C. Stoeckl, S. Dalton, L. Folnsbee, M. J. Guardalben, R. Jungquist, J. Puth, M. J. Shoup III, D. Weiner, and J. D. Zuegel, J. Phys. IV France **133**, 75 (2006).

50. D. H. Froula, J. S. Ross, L. Divol, N. Meezan, A. J. MacKinnon, R. Wallace, and S. H. Glenzer, Phys. Plasmas **13**, 052704 (2006).

51. P. B. Radha, T. J. B. Collins, J. A. Delettrez, Y. Elbaz, R. Epstein, V. Yu. Glebov, V. N. Goncharov, R. L. Keck, J. P. Knauer, J. A. Marozas, F. J. Marshall, R. L. McCrory, P. W. McKenty, D. D. Meyerhofer, S. P. Regan, T. C. Sangster, W. Seka, D. Shvarts, S. Skupsky, Y. Srebro, and C. Stoeckl, Phys. Plasmas **12**, 056307 (2005).

52. D. H. Froula, I. V. Igumenshchev, D. T. Michel, D. H. Edgell, R. Follett, V. Yu. Glebov, V. N. Goncharov, J. Kwiatkowski, F. J. Marshall, P. B. Radha, W. Seka, C. Sorce, S. Stagnitto, C. Stoeckl, and T. C. Sangster, Phys. Rev. Lett. **108**, 125003 (2012).

53. P. W. McKenty, R. S. Craxton, A. Shvydky, F. J. Marshall, J. A. Marozas, S. Skupsky, D. D. Meyerhofer, and R. L. McCrory, Bull. Am. Phys. Soc. **56**, 341 (2011).

54. I. V. Igumenshchev, D. H. Edgell, D. H. Froula, V. N. Goncharov, T. J. Kessler, F. J. Marshall, R. L. McCrory, P. W. McKenty, D. D. Meyerhofer, D. T. Michel, T. C. Sangster, W. Seka, and S. Skupsky, "Improved Performance in Direct-Drive Implosions Using Beam Zooming," to be submitted to Physical Review Letters.

55. T. J. B. Collins, J. A. Marozas, K. S. Anderson, R. Betti, R. S. Craxton, J. A. Delettrez, V. N. Goncharov, D. R. Harding, F. J. Marshall, R. L. McCrory, D. D. Meyerhofer, P. W. McKenty, P. B. Radha, A. Shvydky, S. Skupsky, and J. D. Zuegel, Phys. Plasmas **19**, 056308 (2012).

56. I. V. Igumenshchev, D. H. Froula, D. H. Edgell, V. N. Goncharov, T. J. Kessler, F. J. Marshall, R. L. McCrory, P. W. McKenty, D. D. Meyerhofer, D. T. Michel, T. C. Sangster, W. Seka, and S. Skupsky, "Laser Beam Zooming to Mitigate Cross-Beam Energy Losses in Direct-Drive Implosions," to be submitted to Physical Review Letters.

57. D. H. Froula, I. V. Igumenshchev, A. Shvydky, J. H. Kelly, J. D. Zuegel, E. Hill, and V. N. Goncharov, "Mitigation of Cross-Beam Energy Transfer: Implicaitons of Two-State Optical Zooming on OMEGA," to be submitted to Plasma Physics and Controlled Fusion.

58. P. W. McKenty, V. N. Goncharov, R. P. J. Town, S. Skupsky, R. Betti, and R. L. McCrory, Phys. Plasmas **8**, 2315 (2001).

59. *LLE Review Quarterly Report* **79**, 121, Laboratory for Laser Energetics, University of Rochester, Rochester, NY, LLE Document No. DOE/SF/19460-317, NTIS Order No. DE2002762802 (1999).

60. B. Yaakobi, P.-Y. Chang, A. A. Solodov, C. Stoeckl, D. H. Edgell, R. S. Craxton, S. X. Hu, J. F. Myatt, F. J. Marshall, W. Seka, and D. H. Froula, Phys. Plasmas **19**, 012704 (2012).

61. D. H. Froula, B. Yaakobi, S. X. Hu, P.-Y. Chang, R. S. Craxton, D. H. Edgell, R. Follett, D. T. Michel, J. F. Myatt, W. Seka, R. W. Short, A. Solodov, and C. Stoeckl, Phys. Rev. Lett. **108**, 165003 (2012).

62. K. Y. Sanbonmatsu *et al.*, Phys. Rev. Lett. **82**, 932 (1999).

63. R. Yan, C. Ren, J. Li, A. V. Maximov, W. B. Mori, Z. M. Sheng, and F. S. Tsung, Phys. Rev. Lett. **108**, 175002 (2012).

64. V. A. Smalyuk, R. Betti, J. A. Delettrez, V. Yu. Glebov, D. D. Meyerhofer, P. B. Radha, S. P. Regan, T. C. Sangster, J. Sanz, W. Seka, C. Stoeckl, B. Yaakobi, J. A. Frenje, C. K. Li, R. D. Petrasso, and F. H. Séguin, Phys. Rev. Lett. **104**, 165002 (2010).

65. S. X. Hu, G. Fiksel, V. N. Goncharov, S. Skupsky, D. D. Meyerhofer, and V. A. Smalyuk, Phys. Rev. Lett. **108**, 195003 (2012).

66. G. Fiksel, S. X. Hu, V. N. Goncharov, D. D. Meyerhofer, T. C. Sangster, V. A. Smalyuk, B. Yaakobi, M. J. Bonino, and R. Jungquist, Phys. Plasmas **19**, 062704 (2012).